Steady and Oscillatory Lorentz-Force-Induced Transport and Digitization of Two-Phase Microflows

Joydip Chaudhuri,[1] Tapas Kumar Mandal,[1,2] and Dipankar Bandyopadhyay[1,2,*]

[1]*Department of Chemical Engineering, Indian Institute of Technology Guwahati, Assam 781039, India*
[2]*Centre for Nanotechnology, Indian Institute of Technology Guwahati, Assam 781039, India*

We explore pumping and digitization of two-phase flow patterns inside a microchannel with the help of a unidirectional and oscillating Lorentz force. For this purpose, an electric field has been coupled with an oscillating (or unidirectional) magnetic field to generate a sinusoidal (or unidirectional) Lorentz force in the channel filled with a pair of Newtonian, immiscible, and electrically conducting fluids. Application of the steady or oscillating Lorentz force is found to enhance the throughput of a pressure-driven flow in conjunction with the mixing of the phases by creating discrete and miniaturized flow structures. Numerical simulations show that the application of Lorentz force in an oil-water stratified flow leads to the digitization of the flow patterns together with enhanced transport due to the magnetohydrodynamic pumping of the fluids. The size and frequency of the flow patterns and the throughput of the flow can be noninvasively altered by tuning the intensity of the electric or magnetic field, frequency of the magnetic field, and fluid properties. An oscillatory Lorentz force with periodic change in direction can lead to time-periodic forward and backward motions of the fluids to prompt a unique reciprocating motion of the flow features while they translate along the channel. The oscillation frequency of some of the flow features is found to follow a linear correlation with the frequency of the magnetic field suitable for pumping applications. The proposed pumping and digitization strategies can be of significance in the design and development of next-generation microscale reactors, mixers, pumps, and microelectromechanical systems (MEMS) devices.

I. INTRODUCTION

Digitization of flow patterns into morphologies with relatively higher surface area to volume ratio inside microfluidic devices has shown significant potential in improving the proficiency of a number of cutting-edge applications. These include microreactors [1–3], bio-analysis tools [4,5], microelectromechanical systems (MEMS) [6,7], therapeutic or diagnostic devices [8,9], emulsifiers [10,11], and energy harvesters [12]. The studies related to the precise control on the generation, actuation, movement, and throughput of diverse flow patterns at different time and length scales are also of fundamental importance because a better understanding of the complex physics associated with them can help in expanding their domains of applicability [13–19]. In particular, it is now well understood that the mass, momentum, and heat transfers inside highly confined microsystems are often limited by diffusive length and time scales, which restrict their efficiency and applicability [20–23]. The studies on the creation and applications of microscale gas bubbles or liquid droplets involving gas-liquid [24–26] or liquid-liquid [27,28] flows have revealed that the use of the regular pressure-driven flows in the commercial processes are largely limited by their weaker transport properties and smaller throughput. Thus, much research activity has been observed in the recent past, which involves the enhancement of the transport features through the digitization of flow patterns inside the microfluidic devices [20–32].

For example, the externally applied fields have been employed to disrupt the regular pressure-driven flow patterns to improve the transport properties [33–45]. The noninvasive integration of the applied dc and ac electric fields are found to effectively alter the balance of the capillary, inertial, gravitational, and viscous forces in the pressure-driven microflows to improve the mass, momentum, and heat transfer as well as throughput. The additional electrohydrodynamic (EHD) stresses at the surface or interface due to the accumulation of either bound or free charges can lead to facile deformation, disruption, or actuation of the flow patterns [42–45]. Apart from the electric fields, the transportation of fluids through the lab-on-a-chip devices is achieved by the use of magnetohydrodynamics (MHD) flows [46–49]. In particular, the application of Lorentz

————
*dipban@iitg.ac.in

force provides the added flexibility to maneuver the throughput along with tuning the surface-area-to-volume ratio by the change of flow patterns in the microdevices [50–55]. The use of Lorentz force for pumping also enables facile *in situ* flow reversibility with the change in the direction of the electric or magnetic field in a noninvasive manner in the absence of any moving mechanical parts. Further, the use of Lorentz force in the multiphase flow patterns is expected to have some of the following distinct differences: (i) the force can be applied in any direction [46,51]; (ii) the requirement of the electric field is much lower (higher) leading to a lower (higher) cost of operations [47,51,53]; and (iii) the coupled influence of the electric and magnetic fields enables the disruption of the flow patterns at a much lower applied force (approximately 1 kN) [53]. However, there is hardly any research that explores the salient features of the Lorentz-force-driven transportation of a two-phase flow inside a microchannel and the subsequent flow patterns.

In the present study, we computationally explore the salient features of Lorentz-force-induced transportation and digitization of the two-phase flows inside a microfluidic channel. The schematic diagram in Fig. 1 shows the typical geometry chosen for the computational fluid dynamic (CFD) simulations. It is well known that most of the finite-difference, finite-volume, or finite-element-based CFD frameworks employ volume of fluid (VOF) [56], volume of fluid coupled with level set (CLSVOF) [57], phase field [42,43,45,58,59], level set [44,57,60,61], and Lattice-Boltzmann [62] methods to accurately track the deforming interface of the multiphase flow patterns. Here, we employ a robust and accurate level set method [44,61] as the interface tracking method integrated with a finite-element method to uncover the coupled influence of the electric and magnetic fields of the Lorentz force on the evolution of the flow patterns. The computational framework has been effectively tuned to capture the fluid transport of a pair of weakly conducting (oil) and conducting (water) liquids and the subsequent spatiotemporal evolution of flow patterns under the influence of the Lorentz force.

The study is initiated with the validation of the computational results against the analytical ones related to the Lorentz-force-induced steady and fully developed plane Poiseuille flows. Following this, a series of CFD simulations uncover strategies to improve the throughput of a Lorentz-force-driven two-phase flow inside the channel. In the process, the conditions for the digitization of the two-phase flow patterns inside the channel are uncovered under the influence of a unidirectional or oscillatory Lorentz force direction, as schematically shown in Fig. 1. The results reported suggest that a unidirectional Lorentz force can be utilized for unidirectional transportation and subsequent digitization of the stratified flows into droplets though the stretching of the interface. In comparison, application of the oscillatory Lorentz force with a periodic
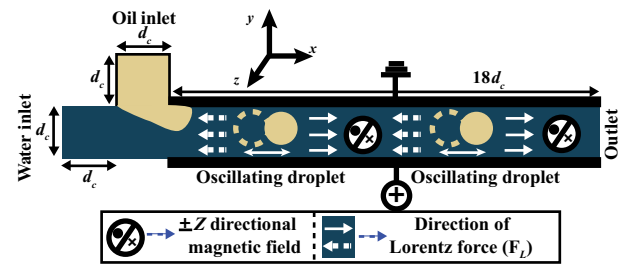

FIG. 1. Schematic diagram of a T microchannel of diameter $d_c = 500\ \mu m$ in which the electric current is flowing in the positive y direction. A steady or oscillating magnetic field is applied toward the positive to negative z direction, which in conjunction with the electric field generates a Lorentz force ($\mathbf{F}_L$) toward the positive to negative x direction. The dimensions are given with respect to d_c.

change in the direction toward upstream and downstream can lead to periodic forward and backward motions of the fluids to engender a unique to-and-fro reciprocating motion of the flow features while they translate across the channel. The noninvasive way of fluid transport with the help of steady or oscillating Lorentz force and the subsequent generation of flow features of higher surface-area-to-volume ratio can improve the efficiency of many microscale applications. Further, the steady and oscillatory throughput of the drops, plugs, or slugs during their migration due to the application of a steady or oscillating Lorentz force can be employed to increase the overall efficiency of heat, mass, and momentum transfers inside microchannels.

II. PROBLEM FORMULATION

A. Governing equations

The two-phase flows of Newtonian, incompressible, and immiscible fluids emulating the dynamics of oil-water systems inside a microchannel can be numerically modeled by solving the following continuity equation along with the Navier-Stokes equations of motion,

$$\nabla \cdot \mathbf{u}_i = 0, \tag{1}$$

$$\rho(\dot{\mathbf{u}}_i + \mathbf{u}_i \cdot \nabla \mathbf{u}_i) = \nabla \cdot (-p_i \mathbf{I} + \mu_i(\nabla \mathbf{u}_i + \nabla \mathbf{u}_i^T)) + \mathbf{F}_{st} + \mathbf{F}_L + \rho \mathbf{g} + \nabla \cdot \mathbf{M}. \tag{2}$$

The subscript 'i' denotes oil ($i = 1$) or water ($i = 2$), the dot symbol over the velocity vector signifies the time derivative, and vector **g** represents the acceleration due to gravity. The gravity is assumed to be acting in the negative y direction of the geometry shown in Fig. 1. For the *i*th fluid, the notation $\mathbf{u}_i$, μ_i, ρ_i, and p_i in Eqs. (1) and (2) represent the velocity vector, dynamic viscosity, density, and pressure, respectively. The force generated due to the interfacial tension is added as $\mathbf{F}_{st}$ in Eq. (2), where subscript *st* denotes

surface tension. The flow of the fluids is accelerated (decelerated) by a positive (negative) x-directional Lorentz force ($\mathbf{F}_L = \mathbf{J} \times \mathbf{B}$) created by the interaction between an externally applied y-directional current density $\mathbf{J}$ and a positive (negative) z-directional magnetic field $\mathbf{B}$. An externally applied electric field potential V_0 generates the electric current density, $\mathbf{J}_i = \sigma_i(\boldsymbol{\psi}_i + \mathbf{u}_i \times \mathbf{B}_i) = \sigma_i(-\nabla V_0 + \mathbf{u}_i \times \mathbf{B}_i)$, where $\boldsymbol{\psi}_i$ is the irrotational electric field. The law of conservation of current density can be expressed as $\nabla \cdot \mathbf{J}_i = \sigma_i \nabla \cdot (-\nabla V_0 + \mathbf{u}_i \times \mathbf{B}_i) = 0$. When the magnetic field is under sinusoidal rotation, the resulting magnetic flux density is $\mathbf{B}_i = \pm B_{\mathrm{Os}}\hat{k}$, where $B_{\mathrm{Os}} = B_z \sin(2\pi f t)$, B_z and f are the amplitude and frequency of the magnetic field, respectively, and $\hat{k}$ is the unit base vector acting along the positive z direction. Due to the weakly conducting (leaky-dielectric) nature of oil, there will be an additional mechanical stress (Maxwell Stress, $M = [\varepsilon \varepsilon_0 (\boldsymbol{\psi}_i \otimes \boldsymbol{\psi}_i - 0.5(\boldsymbol{\psi}_i \cdot \boldsymbol{\psi}_i)\mathbf{I})]$) generated at the oil-water interface, which is also introduced in Eq. (2).

The spatiotemporal tracking of the deforming oil-water interface is modeled using the level set equation, $\dot{\phi} + \mathbf{u}_i \cdot \nabla \phi = \lambda \nabla \cdot (\delta \nabla \phi - (\phi - \phi^2)(\nabla \phi / |\nabla \phi|))$, where the parameter ϕ is the level set function, which acquires a value of less than zero in oil, greater than zero in water, and zero at the fluid interface [44,57,60,61]. The symbol λ represents the stabilization parameter and δ is the thickness of the diffused interface. The surface tension force in Eq. (2) is evaluated as $\mathbf{F}_{st} = \int_\Gamma \gamma_{12} \kappa \, \mathbf{n} \, dS = \gamma_{12} \kappa \, \nabla \phi = -\gamma_{12}(\nabla \cdot [\nabla \phi / |\nabla \phi|])\nabla \phi$, where γ_{12}, κ, S, and $\mathbf{n}$ denote the interfacial tension, curvature of the interface, line element, and a unit outward normal vector along the fluid interface Γ, respectively. The expression of surface tension force suggests that $\mathbf{F}_{st}$ exists when $\nabla \phi$ is non-zero, which is possible only at the diffused interface between oil ($i = 1$) and water ($i = 2$). Thus, in the level set formulation, although the surface tension force is introduced in the equations of motion, it manifests only at the oil-water interface. The density (ρ), viscosity (μ), permittivity (ε), and conductivity (σ) are calculated as $\alpha(\phi) = [\alpha_1 + (\alpha_2 - \alpha_1)H(\phi)] = \alpha_2[\alpha_r + (1 - \alpha_r)H(\phi)]$, where α can be any of the fluid properties, α_1 and α_2 are constant values of fluid properties, $\alpha_r = \alpha_1 / \alpha_2$, and the Heaviside function is $H(\phi) = (0 \text{ if } \phi < 0)$; $(0.5 \text{ if } \phi = 0)$; $(1 \text{ if } \phi > 0)$. The scaling and the dimensionless equations are provided in Section I of the Electronic Supporting Information (ESI) [63].

B. Boundary conditions

An inlet gauge pressure of P_{in} ($i = 2$) $= 10$ Pa and a normal inflow velocity of $u_1 = 0.1$ mm/s are enforced at the water and oil inlet and at the outlet, a gauge pressure of magnitude 0 Pa along with zero viscous stress boundary condition is set to completely define the problem. The pressure-driven flow originating from the weak pressure

drop imposed helps in initializing and convergence of the problem. The channel walls are considered to be partially wetting, nonslipping, and impermeable, and the equilibrium contact angle θ of a discrete oil drop residing inside a continuous water medium is set to 45° [43]. Constant electric potential boundary conditions are enforced at anode ($V_i = V_0$) and cathode ($V_i = 0$) in such a way that electric current is flowing through the microchannel in the positive y direction. In order to exclude the computational complexities associated with electrolysis and Joule heating, the electric potential at the anode is kept between 0 and 1 V. A constant and unidirectional magnetic field is generated by using a permanent magnet of field intensity $B_z = 0$ to 1 T. An electromagnet with oscillating field B_{Os} of amplitude $B_z = 0$ to 1 T is generated along the positive (or negative) z direction based on the polarity of the electromagnet at a specific time instant. The positive (negative) x-directional Lorentz force $\mathbf{F}_L$ is created due to the perpendicular interaction between the positive y-directional electric field current density $\mathbf{J}$ and positive (negative) z-directional magnetic field B_{Os}. The typical magnitudes of dimensional fluid properties employed in the simulations are $\rho_i = 1000$ kg/m³, $\mu_i = 0.001$ to 0.01 Pa s, $\varepsilon_i = 2.2$ to 80, $\sigma_i = 4 \times 10^{-5}$ to 4 S/m, and $\gamma_{12} = 1$ to 12 mN/m [28]. The upper value of conductivity (4 S/m) corresponds to seawater at 25 °C [46,50].

C. Solution methodology

For the present study, we consider two-dimensional (2D) microchannels of diameter $d_c = 500$ μm and length $l = 10$ mm, as shown in Fig. 1. The electrodes of width $w = 9$ mm are placed throughout the downstream of the microchannel starting from 1 mm from the water inlet. The entire computational domain is then divided into approximately 26 710 triangular elements in order to obtain grid independent solutions. COMSOL™ Multiphysics software has been used to solve the unsteady governing equations and the boundary conditions. The software employs a finite-element formulation having (i) a built-in Galerkin-least-squares (GLS) method stabilized through streamline and crosswind diffusions, (ii) second-order elements for velocity gradient calculations, and (iii) first-order elements for pressure gradient calculations to discretize the non-linear convection-diffusion equations. Subsequently, the segregated predictor-corrector method with incremental pressure correction helps in obtaining the spatiotemporal velocity and pressure profiles for the flow. Further, the backward Euler scheme is utilized for consistent initialization in time and the second-order backward difference method is employed for time marching with an optimal time step size of 10 μs.

It may be noted here that during the pinch off of the flow morphologies, one of the curvature components leads to singularity, which is not possible to address employing

the numerical method employed in this study. In order to address this issue, we introduced a standard diffused interface model in the level set method with an infinitesimal interface thickness of δ [57,60], which provides a finite curvature of approximately $1/\delta$ during the pinch off of the flow morphologies. This methodology helps in removing the numerical singularity during the breakup of the flow morphologies.

The simulations shown here neglect any influence of convection of free charge density. This assumption is valid as long as the time scale of charge relaxation τ_r^i, $\tau_r^i = \varepsilon_0 \varepsilon_i / \sigma_i$, is less than the time scale of fluid flow τ_f^i, $\tau_f^i = d_c(\mu_i/\gamma_{12})$. For example, using the values of the fluid properties presented in Sec. B., τ_r^i for oil (water) is 4.87×10^{-7} s (1.77×10^{-10} s) and τ_f^i for oil (water) is 4.16×10^{-4} s (4.16×10^{-5} s). Since, the parameters show that $\tau_r^i << \tau_f^i$, any influence of free charge density is expected to be negligible.

D. Model validation

For validation of the numerical model presented in this study, we consider two fluid layers of thickness d_i, density ρ_i, viscosity μ_i, and electrical conductivity σ_i confined between two electrodes, as shown in Fig. 2(a). The flow is initially driven by a very weak pressure gradient ($\Delta P = 10$ Pa) coupled with an x-directional Lorentz force generated by the interplay between an externally applied electric field in the y direction $\mathbf{J}$ and a magnetic field in the z direction B_z. The use of a constant magnetic field in the positive z direction ensures that the fluid flow occurs toward the positive x direction driven by a unidirectional Lorentz force. The separation distance between the electrodes is d_c. In order to obtain a fully developed flow inside the parallel electrodes, the length of the same is optimized to be $40 d_c$ after several numerical simulations. A few previous works have shown the analytical results for the steady state and fully developed velocity profiles of the Lorentz-force-induced plane Poiseuille flows at different viscosity ratio ($\mu_r = \mu_1/\mu_2$), layer thickness ratio ($d_r = d_1/d_2$), and conductivity ratio ($\sigma_r = \sigma_1/\sigma_2$) [50].

The velocity profiles u_i for the two fluid layers, which are obtained from the present numerical model, are compared and contrasted with these analytical results [50]. Plots 2(b)–(d) clearly suggest the accuracy of the numerical model in predicting the same. The lines (solid, evenly broken, and unevenly broken) in these plots represent the solutions from the analytical expression [50] while the discrete points (square, triangle, and circular symbols) show the numerical results. The mismatch of the velocities at the fluid interface ($y = 0$) can be attributed to the consideration of a deforming interface in numerical simulations as compared to their analytical counterpart.

III. RESULTS AND DISCUSSION

A. Unidirectional Lorentz force

External field induced microflows and subsequent generation of the discrete flow patterns inside the highly confined microchannel geometries are found to be a better alternative than the conventional pressure-driven multiphase flows due to their capacity for enhanced heat, mass, and momentum transfer [27–40]. Here, we demonstrate some of the unexplored pathways to control and expedite throughputs inside such systems, which also lead to the formation of discrete flow structures. It may be noted here that the geometry employed in all the following simulations is as shown in Fig. 1.

Figure 3 shows that the application of an external and unidirectional electromagnetic field B_z can facilitate Lorentz force $\mathbf{F}_L$ induced oil-water flow in the positive x direction. Image (a) in this figure shows a regular pressure-driven flow, which upon application of the Lorentz force leads to the formation of oil slugs ($d_d > d_c$), plugs ($d_d \sim d_c$), and droplets ($d_d < d_c$), with a progressive increase in the Hartmann number as shown in images (b)–(e). Here the Hartmann number (Ha $= d_c B_z \sqrt{\sigma_2/\mu_2}$) signifies the strength of the Lorentz force to the viscous force. Further, the notation d_d is the mean diameter of the flow feature (e.g., drop, slug, or plug) while d_c is the channel diameter and the dimensionless numbers, electric field Bond number Bo and capillary number Ca, are defined as Bo $= \varepsilon_0 \varepsilon_2 d_c \psi^2 / \gamma_{12}$ and Ca $= \mu_2 u_2^{av} / \gamma_{12}$. The origin of these dimensionless numbers from the governing equations has been discussed in detail in Section I of the ESI [63]. The increase in the magnitude of the Lorentz force in the direction of flow assists the two-phase interface to stretch abruptly near the T junction, which in turn generates the discrete oil slugs, plugs, or drops. Images (f)–(i) show the contour plots of Lorentz force acting in the positive x direction with the increase in Ha, which also corresponds to images (b)–(e). The numbers on the images show some typical magnitudes of $\mathbf{F}_L$ in the locations where the tails of the arrows are situated. The images (f)–(i) suggest that, with the increase in Ha, the net Lorentz force in the direction of flow increases from 0.03995 kN/m^3 [$\mathbf{F}_L = 0.04 - 0.00005$ in image (f)] to 18.3 kN/m^3 [$\mathbf{F}_L = 20.2 - 1.9$ in image (i)], which facilitates the digitization of the flow patterns.

Figure 4 shows the typical variations in the various process parameters of the Lorentz-force-driven oil-water in a microchannel. Plot (a) shows the magnitudes of the competing forces, namely, the Lorentz force $\mathbf{F}_L$, capillary force $\mathbf{F}_{st}$, and viscous force $\mathbf{F}_{vis}$ per unit length of the oil-water interface with the variation in the Ha. It may be noted here that the forces are plotted near the T junction at the brink of the breakup of the oil flow features. The plots show that until Ha $\leq 5 \times 10^{-3}$, the magnitudes of $\mathbf{F}_L$ and $\mathbf{F}_{vis}$ remain subdominant as compared to $\mathbf{F}_{st}$, which facilitates
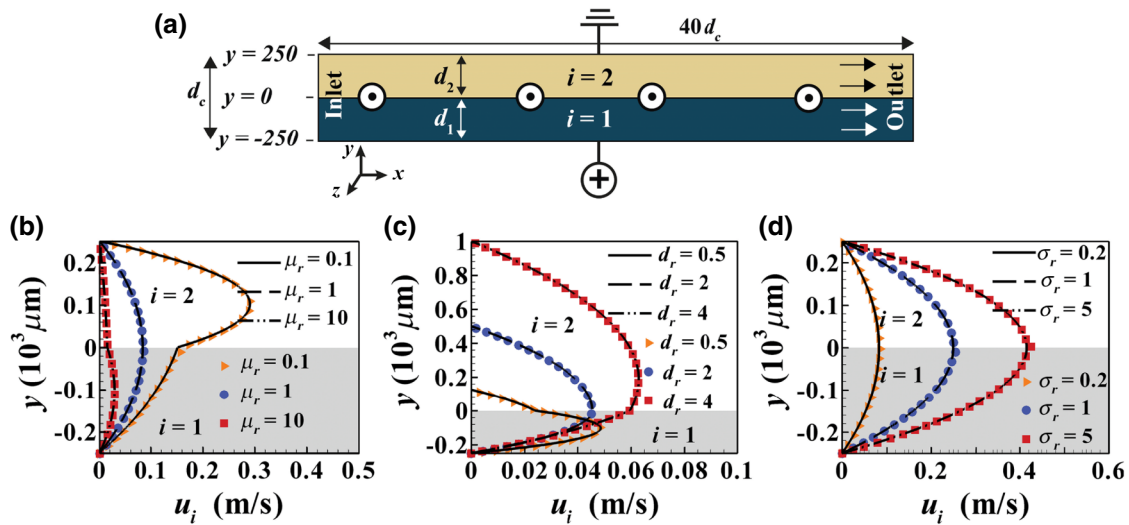
FIG. 2. The schematic diagram (a) shows the geometry of the computational domain $d_c \times 40d_c$ where $d_c = 500$ μm. All the other dimensions are given with respect to d_c. The oil and water layers are denoted by $i = 1$ and 2, respectively, and have thicknesses d_i. The current density, magnetic field, and Lorentz force are acting in the positive y, z, and x directions, respectively. Plots (b)–(d) show the velocity profiles with the variations in $\mu_r \ (= \mu_1/\mu_2)$, $d_r \ (= d_1/d_2)$, and $\sigma_r \ (= \sigma_1/\sigma_2)$, respectively. The solid, evenly broken, and unevenly broken lines (square, circular, and triangle symbols) represent the analytical (numerical) results. The other necessary parameters for the plots are: (b) $\mathrm{Ha}_2 = 0.05$, $d_r = 1$, and $\sigma_r = 0.2$; (c) $\mathrm{Ha}_2 = 0.05$, $\mu_r = 4$, and $\sigma_r = 0.2$; and (d) $\mathrm{Ha}_2 = 0.05$, $d_r = 1$, and $\mu_r = 1$. In plots (b)–(d), $\rho_r = \rho_1/\rho_2 = 1$, $\gamma_{12} = 10$ mN/m, and the Hartmann number is defined as $\mathrm{Ha}_2 = d_2 B_z \sqrt{\sigma_2/\mu_2}$.

the formation of slugs or bigger plugs with relatively lower surface-area-to-volume ratios. Beyond a critical strength of Lorentz force ($\mathrm{Ha} \geq 5 \times 10^{-3}$, $\mathbf{F}_L > \mathbf{F}_{st}$), formation of the flow patterns with higher surface-area-to-volume ratio are observed. The product of the total number of droplets produced per second (droplet frequency, D_f) with the perimeter of the droplet ($= \pi d_d$) can give an idea of the increase in the surface-area-to-volume ratio, which we define as the interfacial length L. This parameter gives a general idea

of the availability of the interfacial area for heat, mass, or momentum transfer. Plot (b) shows the variation of L with Ha, which suggests more than seven-fold increase in the available interfacial length due to the digitization of the flow patterns with the increase in Ha.

Apart from the increase in the surface-area-to-volume ratio, we also observe a significant increase in the throughput under the influence of the steady Lorentz force. Plots (c) and (d) show the monotonic increase in volumetric flow
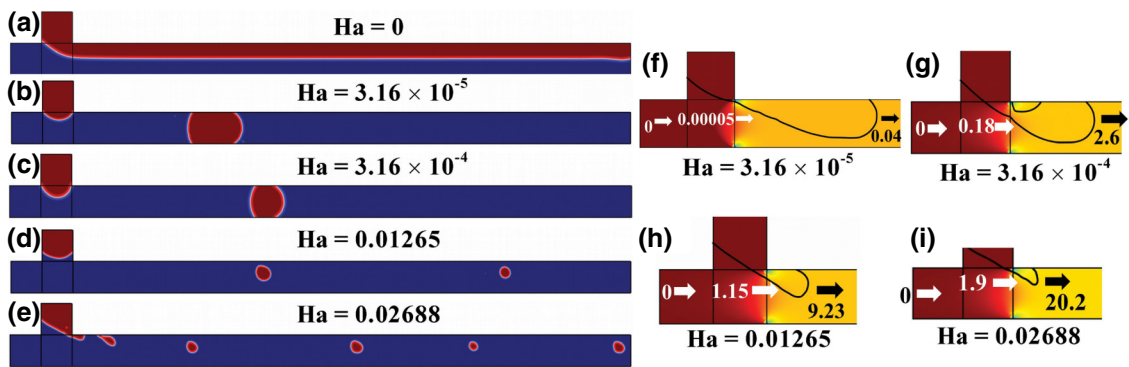

FIG. 3. Images (a)–(e) show the phenomena where a unidirectional Lorentz force ($\mathbf{F}_L$) disrupts a pressure-driven stratified flow to discrete flow features such as slug [$d_d > d_c$, image (b)], plug [$d_d \sim d_c$, image (c)] and droplets [$d_d < d_c$, images (d),(e)]. Images (f)–(i) show the magnified view of the oil-water interface (solid lines) near the T junction of the microchannel in which the contours show the magnitude of $\mathbf{F}_L$ (kN/m^3) at the time of breakup. Lighter (Darker) shades in the colored contours indicate regions with higher (lower) force. The numbers on the images show some typical magnitudes of $\mathbf{F}_L$ in the locations where the tails of the arrows are situated. The other parameters employed in these simulations are $u_1 = 0.1$ mm/s, $\mu_r = 10$, $\sigma_r = 10^{-5}$, $\mathrm{Ca} = 2.604 \times 10^{-4}$, $\mathrm{Bo} = 0$ for (a), and $\mathrm{Bo} = 4.72213 \times 10^{-4}$ for (b)–(e).
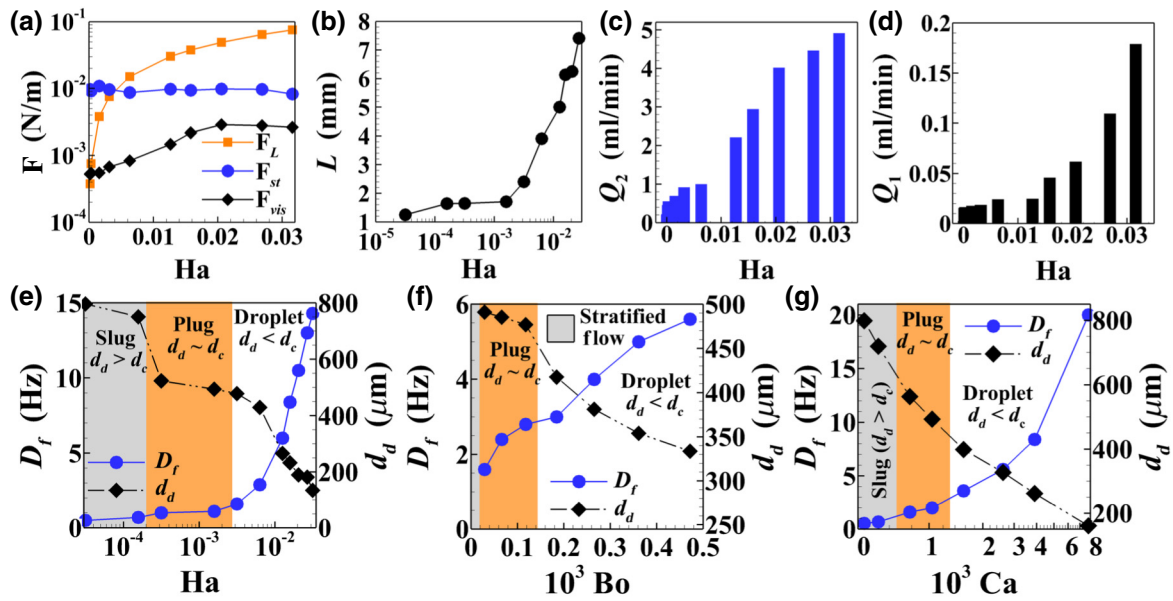
FIG. 4. Plot (a) shows the variation of $\mathbf{F}_L$ (square symbols), capillary force ($\mathbf{F}_{st}$, circular symbols), and viscous force ($\mathbf{F}_{vis}$, diamond symbols) along the interface with Ha. Plot (b) shows the variation in the total available interfacial length L of the flow features with Ha. Plots (c) and (d) show the variations in flow rates Q_i of water ($i = 2$) and oil ($i = 1$) with Ha. Plots (e)–(g) show the variations in frequency of ejection of the flow patterns – droplet or plug or slug (D_f – circular symbols, left y axis) and mean diameter (d_d – diamond symbols, right y axis) with the variations in the Ha, Bo, and Ca, respectively. The regions of droplet, plug, slug, or stratified formation are depicted on the image at different Ha, Bo, and Ca. The other parameters employed in these simulations are $u_1 = 0.1$ mm/s, $\mu_r = 10$, $\sigma_r = 10^{-5}$, Ca $= 2.604 \times 10^{-4}$ for (a)–(f), Ha $= 0.0158$ for (f)–(g), Bo $= 4.72213 \times 10^{-4}$ for (a)–(e) and (g).

rate Q_i with Ha of water ($i = 2$) and oil ($i = 1$) phases. An increase in Ha to 0.032 can increase the base flow rate by 25 times leading to a flow rate of approximately 5 ml/min (approximately 0.18 ml/min) for a less (more) viscous water (oil) phase. Plots (e)–(g) show the sensitivities of the magnetic field intensity B_z, electric field intensity ψ, and interfacial tension γ_{12} to the aforementioned phenomena in terms of the dimensionless parameters Ha, Bo, and Ca. The plots suggest the variations in the ejection frequency D_f and mean diameter d_d of the flow features with Ha, Bo, and Ca. The plots also show the parametric domains of the different flow morphologies such as the stratified, slug, plug, and droplet. The parameter D_f suggests the overall throughput of the process while d_d shows the extent of miniaturization possible with the process. Plots (e)–(g) clearly show that with the increase in Ha (increase in B_z), Bo (increase in ψ), and Ca (decrease in γ_{12}) the D_f increases and d_d decreases considerably. While the increase in Ca facilitates the miniaturization of the flow features, the increases in Ha and Bo assist in the stretching, deformation, and digitization steps to form smaller flow features with higher throughput. In summary, Figs. 3 and 4 together show the pathways to integrate a noninvasive and unidirectional Lorentz force with the pressure-driven oil-water flows to generate the flow patterns with smaller size, higher surface-area-to-volume ratio, and larger throughput.

B. Oscillating Lorentz force

We have discussed the salient features of the unidirectional Lorentz-force-induced oil-water flows. However, a sinusoidally varying Lorentz force can be another efficient alternative to pump, mix, stir, or shake microfluidic flow patterns. In the following simulations, the direction of the magnetic field has been varied from the negative to positive z direction in a time-periodic manner as $B_{Os} = B_z \sin(2\pi ft)$, where B_z and f are the amplitude and frequency of the magnetic field, respectively. The sinusoidal oscillation of the magnetic field leads to a Lorentz force, which also periodically changes its magnitude and direction toward the upstream and downstream directions at a frequency f with the variation in time. Supporting Video 1 shows one such a spatiotemporal evolution of the oil-water flow and the subsequent profiles of the reciprocating time-periodic motion under the influence of the oscillating Lorentz force [63]. Figure 5(a) shows the variation in the velocity profile of water u_2 at the outlet for a time period of $t = 0$ to 0.5 s where $B_z = 0.05$ T and $f = 20$ Hz. Under these conditions, since we observe the oil-phase to be the dispersed phase, the variations of the velocity profile of the continuous water phase u_2 in the outlet at different time intervals are shown. In this case, the amplitude of the oscillating magnetic field is deliberately kept low to stimulate a weak water flow through the channel while a relatively higher
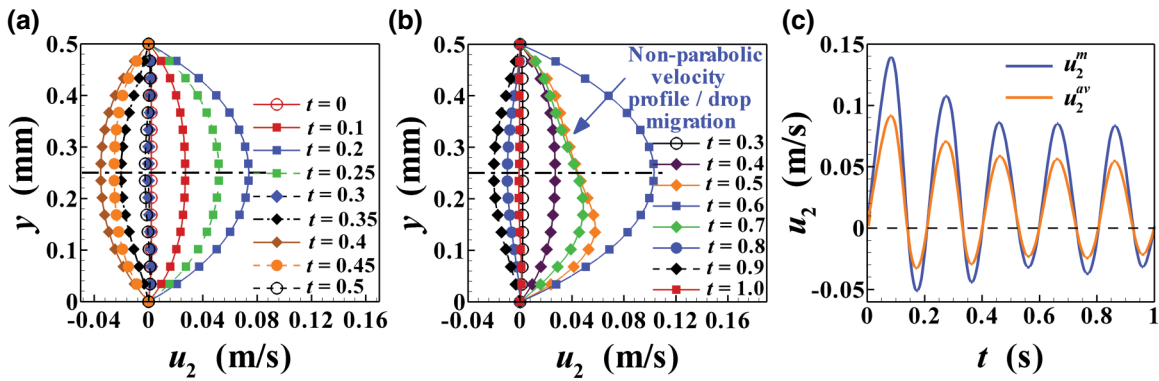
FIG. 5. Plots (a) and (b) show the variations of symmetric and asymmetric velocity profiles of the water phase u_2 at the outlet for the time intervals $t = 0-0.5$ s and $t = 0.3-1.0$ s, respectively. Plot (c) shows the variations in the maximum (darker line, u_2^m) and average (lighter line, u_2^{av}) velocities with time t for the case presented in plot (b). For plot (a) $B_z = 0.05$ T and $f = 20$ Hz while for plots (b) and (c) $B_z = 0.5$ T and $f = 5$ Hz. The other parameters employed are $u_1 = 0.1$ mm/s, $\rho_r = 1$, $\mu_r = 10$, $\sigma_r = 10^{-5}$, and $\gamma_{12} = 2$ mN/m.

frequency ensures that the direction of the field changes more frequently.

Plot 5(a) and supporting Video 1 suggest that initially ($t = 0$ s), the outlet velocity of water is almost negligible. Following this, in the beginning of the forward half-cycle, as the magnitude of the Lorentz force ($\mathbf{F}_L$) increases in the positive x-direction with the progress in time, the net throughput of the oil-water flow increases, as shown by the profiles corresponding to $t = 0.1$ s to 0.2 s. Thereafter, at the end of the forward half-cycle, as the magnitude of the Lorentz force ($\mathbf{F}_L$) decreases in the positive x direction with time, the net throughput of the oil-water flow decreases during the time interval $t = 0.2$ s to 0.3 s. After this, in the beginning of the reverse half-cycle, as the magnitude of the Lorentz force ($\mathbf{F}_L$) increases with time in the negative x direction, the throughput increases in the reverse direction during the time interval $t = 0.3$ s to 0.4 s. During the final phase of the reverse half-cycle, as the magnitude of the Lorentz force $\mathbf{F}_L$ temporally decreases in the negative x direction, the reverse throughput also decreases during the time interval $t = 0.4$ s to 0.5 s. The cycle discussed above keeps repeating in a time-periodic manner with the temporal variation in the direction and magnitude of $\mathbf{F}_L$, which eventually produces interesting oil-water flow morphologies moving to-and-fro (reciprocating) while they migrate across the channel.

The conditions for plot (a) ensure that the flow is essentially single phase and there are no oil drops migrating across the domain. In comparison, the conditions for plot (b) ensure that the oil droplets migrate through the channel when $B_z = 0.5$ T and $f = 5$ Hz, as shown by supporting Video 2 [63]. In this case, the amplitude of the oscillating magnetic field is kept higher than that in plot (a) to stimulate a stronger Lorentz force while a relatively lower frequency ensures that the force acts for a longer duration in a particular direction facilitating the drop formation. The plot suggests that the velocity profiles in the forward and

reverse cycles of the Lorentz-force-induced motion remain similar to that in plot (a) with the exception of the appearance of asymmetric and nonparabolic velocity profiles at time intervals $t = 0.5$ s and 0.7 s. The asymmetry in the profile has its origin in the migration of the oil drop through the outlet during the aforementioned time interval.

Plot (c) shows the variations in the maximum (darker line, u_2^m) and average (lighter line, u_2^{av}) velocities with time t for the case shown in plot (b). The curves suggest that, in this situation, the time-periodic variations of u_2^{av} and u_2^m in each cycle of forward and reverse flows are initially large and progressively attenuate to a steady value. The unsteady time-periodic variations of u_2^{av} and u_2^m can be attributed to situations where dispersed oil droplets are generated in the water phase and subsequently transported downstream. Interestingly, the largest magnitudes of $u_2^m \sim 0.05$ m/s and $u_2^{av} \sim 0.03$ m/s at $t = 0.18$ s during the reverse flow cycle is found to be about three times less than the same in the forward cycle, $u_2^m \sim 0.15$ m/s and $u_2^{av} \sim 0.09$ m/s at $t = 0.1$ s. This is because the simulations are performed with a weak pressure-driven forward flow, which contributes to the larger magnitudes of u_2^{av} and u_2^m during the forward cycle. Figure 5 indicates that time-periodic variations in the magnitude and direction of a magnetic field can lead to a reciprocating Lorentz force, which can induce a time-periodic reciprocating motion inside an oil-water flow. The figure also indicates that the throughput and the flow morphologies can be tuned by varying the intensity and frequency of the externally applied electromagnetic field.

Images (a)–(j) in Fig. 6 and supporting Video 3 show the typical flow behaviors and the subsequent morphologies of the oil-water flow inside a microchannel driven by the oscillating Lorentz force [63]. In this case, the flow is facilitated by the oscillating magnetic field with $B_z = 0.5$ T and $f = 10$ Hz, which ensures that a strong and oscillating Lorentz force $\mathbf{F}_L$ is in action. The white arrows in
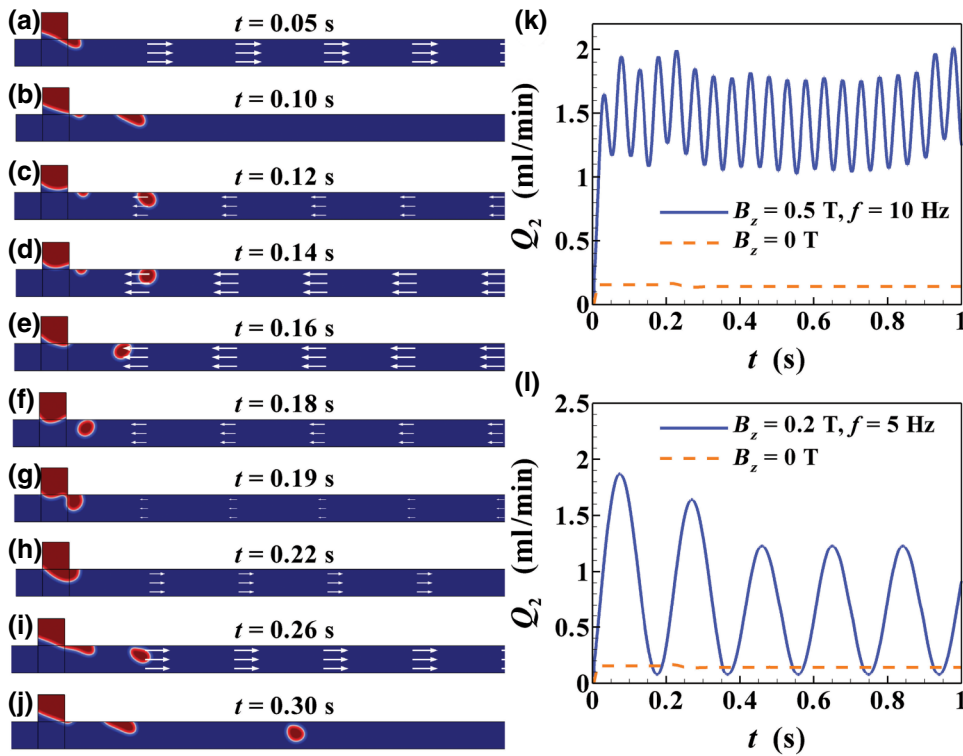
FIG. 6. Images (a)–(j) show the spatiotemporal migration of oil droplets when $B_z = 0.5$ T and $f = 10$ Hz. Plot (k) shows the variation in the flow rate of water Q_2 with time t when $B_z = 0.5$ T and $f = 10$ Hz and when $B_z = 0$. Plot (l) shows the variation in Q_2 with t when $B_z = 0.2$ T and $f = 5$ Hz and when $B_z = 0$. The other parameters employed in the simulations are $u_1 = 0.1$ mm/s, $\rho_r = 1$, $\mu_r = 10$, and $\sigma_r = 10^{-5}$. The parameter $\gamma_{12} = 2$ mN/m for images (a)–(k) and 5 mN/m for image (l).

the images show the direction of the Lorentz force at any time instant unless mentioned otherwise. The images and the video show the following stages of the evolution; (i) images (a)–(c) show the formation of the droplet and accelerated ejection in the forward half-cycle with increasing velocity; (ii) images (c)–(e) show the slowing down of the droplet during the forward half-cycle with reducing velocity; (iii) images (e)–(g) show the upstream motion of the droplet toward the inlets during the reverse half-cycle with increasing velocity; and (iv) images (g)–(h) show the coalescence of the droplet with the oil-pool at the oil inlet during the reverse half-cycle with decreasing velocity. The conditions employed in the simulations also ensure that while one of the oil droplets coalesces with the oil pool at the vertical inlet, the other one is ejected out of the domain and shows oscillatory motion during its travel all along the microchannel, as shown by images (i)–(j). In the time-periodic steady state of evolution, the aforementioned steps keep repeating with time. The behavior is analogous to a fluidic 'ratchet' wherein the fluid flow provides the forward bias to move the droplet toward the outlet while the magnetic field provides an oscillatory action.

Plots (k) and (l) show the periodic variations in water flow rates Q_2 with time t for different B_z and f. The plots show that when the oil phase discretizes into smaller flow structures like droplets [images (a)–(j)] inside the continuous water phase, the Q_2 (solid line) varies periodically with time between 1 to 2 ml/min to maintain an average forward flow rate of $Q_2^{av} \sim 1.5$ ml/min, as shown in plot (k). The

broken line in plot (k) shows the base flow rate (approximately 0.15 ml/min) when the flow of both the phases (oil and water) are driven by the weak pressure gradient only. The plot suggests that the Lorentz force can increase the flow rate by about 10 times emulating the performance of a reciprocating micropump. The Q_2^{av} can be tuned by changing the maximum intensity B_z and frequency f of the oscillating magnetic field. For example, plot (l) shows that $Q_2^{av} \sim 0.73$ ml/min when $B_z = 0.2$ T and $f = 5$ Hz.

Importantly, the time-periodic lateral oscillations of the drops not only enforce a reciprocating pumping action but also help in mixing multicomponent systems. Figure 7 and supporting Videos 4 and 5 show that apart from droplets the other types of flow features such as plugs or slugs can also be generated by tuning the Lorentz force with the variations in B_z and/or f [63]. Again, the images and the videos show the following stages of the evolution; (i) images (a)–(c) show the formation of the plug or slug and accelerated ejection in the forward half-cycle with increasing velocity; (ii) images (c)–(e) show the slowing down of the plug or slug during the forward half-cycle with reducing velocity; (iii) images (e)–(g) show the upstream motion of the plug or slug toward the inlets during the reverse half-cycle with increasing velocity; and (iv) images (g)–(h) show the coalescence of the plug or slug with the oil pool at the oil inlet during the reverse half-cycle with reducing velocity. Another slug is ejected out of the domain showing to-and-fro oscillating motion during its travel all along the microchannel as shown by images (h)–(i). Remarkably enough, these flow features also show
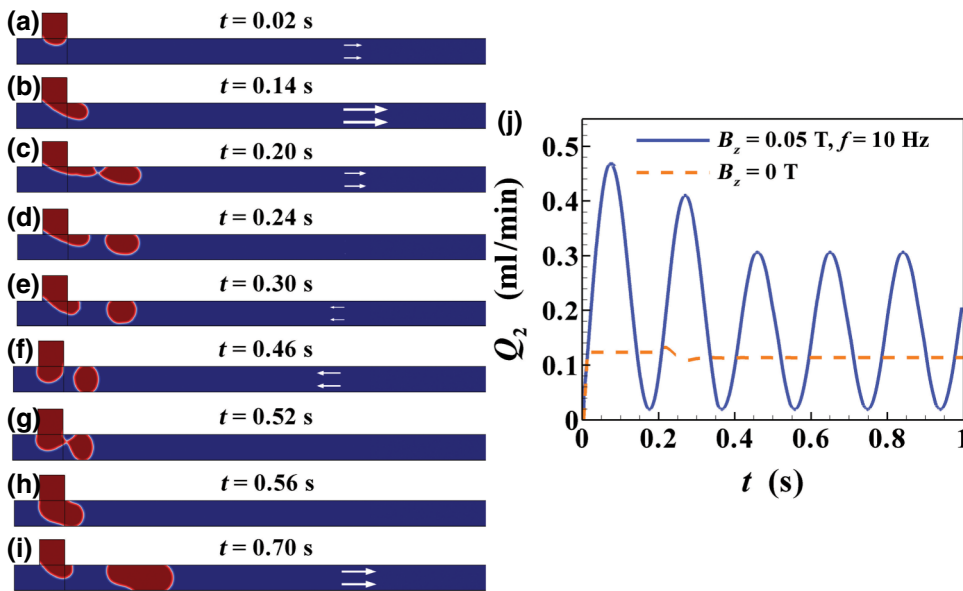
FIG. 7. Images (a)–(i) show the spatiotemporal migration of oil slugs when $B_z = 0.05$ T and $f = 10$ Hz. Plot (j) shows the variation in the flow rate of water Q_2 with time t when $B_z = 0.05$ T and $f = 10$ Hz and when $B_z = 0$ T. The other parameters employed in the simulations are $u_1 = 0.1$ mm/s, $\rho_r = 1$, $\mu_r = 10$, and $\sigma_r = 10^{-5}$. Parameter $\gamma_{12} = 4$ mN/m for images (a)–(j).

periodic variations of Q_2 with t resembling the flows with droplet morphologies as shown in plot (j).

Figures 4–7 concisely show some very important features of the influence of the oscillating Lorentz force in the generation of reciprocating pump action inside a microchannel. While the oscillating Lorentz force acting on the conducting continuous phase water generates a reciprocating pump action in a noninvasive manner, the oscillations of the incompressible droplets or slugs or plugs act as the reciprocating pistons or stirrers to enhance the pumping and mixing activity. The results suggest that the throughput of the flow inside the channel can be precisely controlled in a noninvasive manner by simple alterations in the amplitude and frequency of the oscillating magnetic field. Further, the figures suggest that the same system can be employed for developing flow morphologies with higher surface-area-to-volume ratio such as the droplets. It should be noted here that different flow features, such as slug, plug, and droplets have been created with magnetic field intensities as low as 0.001 T (slug), 0.01 T (plug), and 0.2 T (droplets), which can be easily implemented in the experiments. The inherent oscillations reported in the flow of the continuous water and dispersed oil phases can help in improving the heat, mass, and momentum transfer characteristics of various types of microfluidic flows.

The time-periodic sinusoidal variation in the applied magnetic field ensures the alteration in the magnitude and direction of the Lorentz force, which eventually oscillates the motions of the droplets, plugs, or slugs while they translate across the channel. In such a scenario, the periodic undulations experienced by the different flow features are also different depending on their size and shape. In order to explore these aspects, in this study, we define a couple of parameters such as the (i) net displacement of a flow feature during a cycle, $N_d = d_{sf} - d_{sb}$, and (ii)

approach of a flow feature, $A = d_{sf}/d_{sb}$. Plots (a) and (b) in Fig. 8 show the variation of N_d and A with f for the droplets and slugs, respectively. The plots suggest that the droplets tend to have larger N_d and A than the slugs inside the microchannel. The miniaturized droplets with higher surface-area-to-volume ratio move more quickly with less residence time inside the channel leading to a larger oil throughput. In comparison, the relatively larger slugs show relatively slower ($A \sim 1$) reciprocating migration inside the microchannel, which can be exploited for pumping, stirring, or mixing applications. It can also be visualized from plots (a) and (b) that at a maximum frequency of $f = 1$ kHz of the frequency domain $f = 0$–1 kHz, N_d (approximately 0) becomes almost negligible, which cannot be cultivated as a quantifiable droplet displacement for feasible droplet actuation-based practical applications, thus eliminating the logic for further increasing the frequency of the oscillating magnetic field.

Supporting Videos 6 and 7 show the oscillating motions of droplet and slug, respectively, in the forward and reverse directions for four complete cycles of time-periodic variation in the Lorentz force [63]. A series of such simulations reveals that the oscillations of these flow features vary considerably with the frequency f of the time-periodic magnetic field. In order to characterize this behavior, we consider the following things: (i) during the forward half-cycle, the flow feature moves toward the outlet in which the velocity toward the downstream direction initially increases and then decreases with $\mathbf{F}_L$; (ii) during the reverse half-cycle, the flow feature moves toward the inlets in which the upstream velocity initially increases and then decreases with $\mathbf{F}_L$; and (iii) a weak pressure-driven flow ($\Delta P = 10$ Pa) ensures that the displacement during the forward half-cycle (d_{sf}) is always greater than the displacement during the reverse half-cycle (d_{sb}). For example,
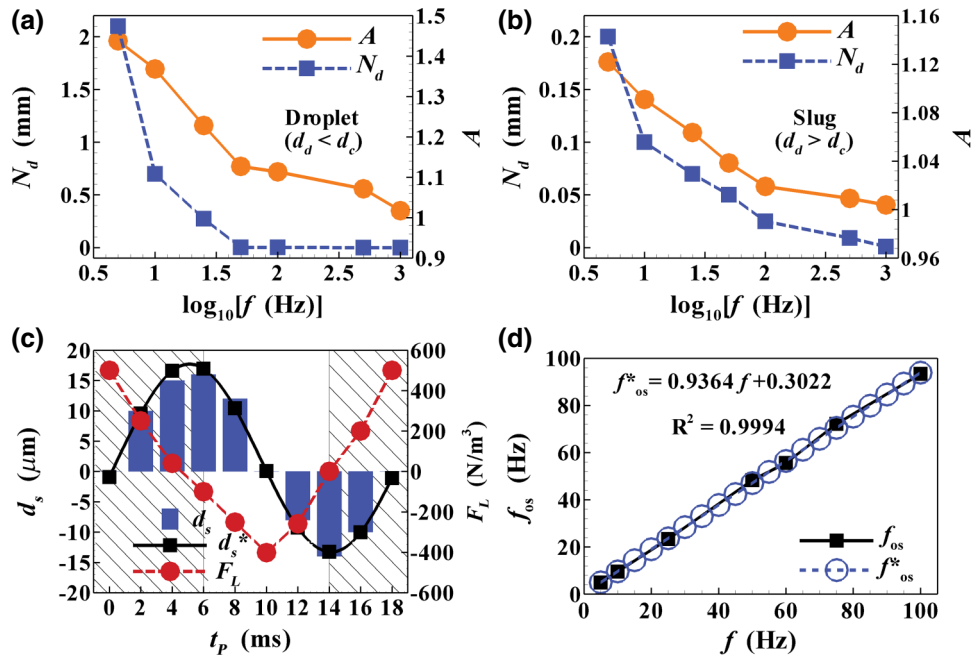
FIG. 8.   Plot (a) shows the variations of net displacement (N_d – square symbols, left y axis) and approach (A – circular symbols, right y axis) of oil droplets with frequency f after a complete forward and reverse cycle. Plot (b) is a repeat of plot (a) for the oil slugs. Plot (c) shows the variation in displacement of a slug (d_s – blue bars, left y axis) and corresponding Lorentz force ($\mathbf{F}_L$ – circular symbols, right y axis) during a time period t_P during forward (hashed) and reverse (nonhashed) half-cycles (HC) when $f = 60$ Hz. Plot (d) shows the variation in the oscillation frequency of the slug (f_{os} – square symbols) with f, which leads to a straight line (circular symbols, $f_{os}^* = 0.9364 f + 0.3022$ having an R^2 value of 0.9994). In these plots, Ca $= 2.604 \times 10^{-4}$ for (a) and Ca $= 0.104167$ for (b)–(d). The other parameters employed in the simulations are $u_1 = 0.1$ mm/s, $\rho_r = 1$, $\mu_r = 10$, $\sigma_r = 10^{-5}$, Ha $= 0.0158$, and Bo $= 4.72213 \times 10^{-4}$.

the typical displacement of the slugs (d_s, blue bars) during a time period t_P representing a complete forward and reverse cycle is shown in plot (c) when $f = 60$ Hz. The time period $t_P = 0$–18 ms in the plot represents the time range $t = 491$ to 509 ms of the actual simulation in which one of the full cycles of oscillation of the slug occurs. A generic sine curve [$d_s^* = C \sin(2\pi f_{os} t_P - \varphi) + D$] can be fitted to this dataset quite accurately in order to find out the oscillation frequency of the slug f_{os} in such a situation where C (=15.4995 μm) is the amplitude of the oscillation, f_{os} (= 55.56 Hz) is the oscillation frequency of the slug, φ (= 0.20405 rad) is the phase lag, and D (= 2.2171 μm) is the offset.

The oscillatory Lorentz force and the weak pressure-driven flow both induce inertia to the discrete flow features and the surrounding continuous phase. It can be easily envisaged that, at the time instant when the Lorentz force changes its direction, the inertia associated with the flow structure opposes the same, as shown in supporting Videos 6 and 7. After some time, the Lorentz force overcomes this inertial effect to move the oil droplet or other flow structures in its direction, which is the major reason behind the phase lag between the oscillatory motion of the flow features with Lorentz force. Interestingly, the variations in the Lorentz force $\mathbf{F}_L$ and d_s^* with t_P show behaviors almost

similar to that of a simple harmonic oscillator for the slug flow patterns when $A \sim 1$, as shown in the image (c).

The fitting parameters can be correlated to develop a digital time counter employing the microfluidic systems. For example, plot (d) shows that the variation in oscillation frequency of the slug f_{os} follows a linear correlation with the frequency of the magnetic field f as $f_{os}^* = 0.9364 f + 0.3022$, in the range of $0 \leq f \leq 100$ Hz, where f_{os}^* is the oscillation frequency of the slug obtained from the linear correlation. This correlation can be employed to develop a slug-driven reciprocating pump inside a microchannel due to the uniformity in the amplitude of oscillations in the forward and the reverse cycles of motion stimulated by the time-periodic Lorentz force. However, for the flow features such as droplets ($A \sim 1.5$), we observe that the oscillatory motion with larger (smaller) amplitude toward the downstream (upstream) of the channel during the forward (reverse) cycle, as shown in supporting Video 3, may not be suitable for a pump but can be appropriate for mixing applications.

IV. CONCLUSIONS

In summary, we identify that a constant and unidirectional magnetic field disrupts the interface of a pair

of conducting fluids to produce different types of flow morphologies inside microchannels. Discrete flow features such as droplet, plug, and slug with a higher surface-area-to-volume ratio can be attained with precise control because of the unidirectional nature of the Lorentz force for mixing in multiphase microflows. The study also shows that the shape, size, and frequency of the discrete flow features can be tuned not only by changing the magnitude and/or direction of the externally applied electric or magnetic field, but also by tweaking the inherent fluid parameters such as interfacial tension.

The oscillating Lorentz force originating from the interaction between an externally applied electric current density and a sinusoidal magnetic field is found to change the direction of flow periodically inside the microchannels, which can be utilized for the field induced noninvasive transport and mixing of fluids. In this process, digitization of the flow morphologies into higher surface-area-to-volume ratio droplets, plugs, or slugs enables the improvement in the efficiency of the heat, momentum, and mass transport. While in transport, the oscillations of the flow features (droplets or slugs) follow the almost similar sinusoidal behavior of the oscillating magnetic field with a marginal phase lag. This ensures that an efficient reciprocating pumping activity can be attained employing incompressible droplets by tuning the frequency and amplitude of the externally applied oscillating magnetic field.

The results reported on the transport, actuation, and reversal of fluid flow at a lower power, in the absence of any moving parts and in a noninvasive manner, open up the possibility of their use for state-of-the-art microscale mixing, reactor, and pumping applications with improved heat, mass, and momentum transport capabilities.

ACKNOWLEDGMENTS

---

[1] K. F. Jensen, Microreaction engineering–is small better?, Chem. Eng. Sci. **56**, 293 (2001).

[2] X. Niu, M. Zhang, J. Wu, W. Wen, and P. Sheng, Generation and manipulation of "smart" droplets, Soft Matter. **5**, 576 (2009).

[3] J. D. Tice, H. Song, A. D. Lyon, and R. F. Ismagilov, Formation of droplets and mixing in multiphase microfluidics at low values of the Reynolds and the capillary numbers, Langmuir **19**, 9127 (2003).

[4] H. N. Joensson, and H. A. Svahn, Droplet microfluidics — A tool for single-cell analysis, Angew. Chem. Int. Ed. **51**, 12176 (2012).

[5] V. Taly, D. Pekin, A. E. Abed, and P. Laurent-Puig, Detecting biomarkers with microdroplet technology, Trends Mol. Med. **18**, 405 (2012).

[6] M. A. Burns, B. N. Johnson, S. N. Brahmasandra, K. Handique, J. R. Webster, M. Krishnan, T. S. Sammarco, P. M. Man, D. Jones, D. Heldsinger, C. H. Mastrangelo, and D. T. Burke, An integrated nanoliter DNA analysis device, Science **282**, 484 (1998).

[7] H. Tsuchiya, M. Okochi, N. Nagao, M. Shikida, and H. Honda, On-chip polymerase chain reaction microdevice employing a magnetic droplet-manipulation system, Sens. Actuators B **130**, 583 (2008).

[8] L. Capretto, D. Carugo, S. Mazzitelli, C. Nastruzzi, and X. Zhang, Microfluidic and lab-on-a-chip preparation routes for organic nanoparticles and vesicular systems for nanomedicine applications, Adv. Drug Delivery Rev. **65**, 1496 (2013).

[9] D. Bennet, and S. Kim, Implantable microdevice for peripheral nerve regeneration: Materials and fabrications, J. Mater. Sci. **46**, 4723 (2011).

[10] S. L. Anna, N. Bontoux, and H. A. Stone, Formation of dispersions using "flow focusing" in microchannels, App. Phys. Lett. **82**, 364 (2003).

[11] T. Thorsen, R. W. Roberts, F. H. Arnold, and S. R. Quake, Dynamic Pattern Formation in a Vesicle-Generating Microfluidic Device, Phys. Rev. Lett. **86**, 4163 (2001).

[12] ÁG Marín, W. van Hoeve, P. García-Sánchez, L. Shui, Y. Xie, M. A. Fontelos, J. C. T. Eijkel, A. van den Berg, and D. Lohse, The microfluidic Kelvin water dropper, Lab Chip **13**, 4503 (2013).

[13] P. Garstecki, M. J. Fuerstman, H. A. Stone, and G. M. Whitesides, Formation of droplets and bubbles in a microfluidic T-junction–scaling and mechanism of breakup, Lab Chip **6**, 437 (2006).

[14] R. Ledesma-Aguilar, R. Nistal, A. Hernández-Machado, and I. Pagonabarraga, Controlled drop emission by wetting properties in driven liquid filaments, Nat. Mater. **10**, 367 (2011).

[15] H. Gau, S. Herminghaus, P. Lenz, and R. Lipowsky, Liquid morphologies on structured surfaces: From microchannels to microchips, Science **283**, 46 (1999).

[16] B. Zhao, J. S. Moore, and D. J. Beebe, Surface-directed liquid flow inside microchannels, Science **291**, 1023 (2001).

[17] J. Ou, B. Perot, and J. P. Rothstein, Laminar drag reduction in microchannels using ultrahydrophobic surfaces, Phys. Fluids **16**, 4635 (2004).

[18] A. Günther, and K. F. Jensen, Multiphase microfluidics: From flow characteristics to chemical and materials synthesis, Lab Chip **6**, 1487 (2006).

[19] D. Di Carlo, Inertial microfluidics, Lab Chip **9**, 3038 (2009).

[20] H. A. Stone, A. D. Stroock, and A. Ajdari, Engineering flows in small devices: Microfluidics toward a lab-on-a-chip, Annu. Rev. Fluid Mech. **36**, 381 (2004).

[21] L. Shui, J. C. T. Eijkel, and A. van den Berg, Multiphase flow in microfluidic systems –control and applications of droplets and interfaces, Adv. Colloid Interface Sci. **133,** 35 (2007).

[22] C. N. Baroud, F. Gallaire, and R. Dangla, Dynamics of microfluidic droplets, Lab Chip **10,** 2032 (2010).

[23] C.-X. Zhao, and A. P. J. Middelberg, Two-phase microfluidic flows, Chem. Eng. Sci. **66,** 1394 (2011).

[24] K. A. Triplett, S. M. Ghiaasiaan, S. I. Abdel-Khalik, and D. L. Sadowski, Gas–liquid two-phase flow in microchannels Part I: Two-phase flow patterns, Int. J. Multiphase Flow **25,** 377 (1999).

[25] A. Kawahara, P. M.-Y. Chung, and M. Kawaji, Investigation of two-phase flow pattern, void fraction and pressure drop in a microchannel, Int. J. Multiphase Flow **28,** 1411 (2002).

[26] R. M. Santos, and M. Kawaji, Numerical modeling and experimental investigation of gas–liquid slug formation in a microchannel T-junction, Int. J. Multiphase Flow **36,** 314 (2010).

[27] S. Lecuyer, W. D. Ristenpart, O. Vincent, and H. A. Stone, Electrohydrodynamic size stratification and flow separation of giant vesicles, Appl. Phys. Lett. **92,** 104105 (2008).

[28] S. Timung, V. Tiwari, A. K. Singh, T. K. Mandal, and D. Bandyopadhyay, Capillary force mediated flow patterns and non-monotonic pressure drop characteristics of oil-water microflows, Can. J. Chem. Eng. **93,** 1736 (2015).

[29] S. Torza, R. G. Cox, and S. G. Mason, Electrohydrodynamic deformation and bursts of liquid drops, Philos. Trans. R. Soc. A **269,** 295 (1971).

[30] O. Vizika, and D. A. Saville, The electrohydrodynamic deformation of drops suspended in liquids in steady and oscillatory electric fields, J. Fluid Mech. **239,** 1 (1992).

[31] J. D. Sherwood, Breakup of fluid droplets in electric and magnetic fields, J. Fluid Mech. **188,** 133 (1988).

[32] J. Q. Feng, and T. C. Scott, A computational analysis of electrohydrodynamics of a leaky dielectric drop in an electric field, J. Fluid Mech. **311,** 289 (1996).

[33] O. Ozen, N. Aubry, D. T. Papageorgiou, and P. G. Petropoulos, Monodisperse Drop Formation in Square Microchannels, Phys. Rev. Lett. **96,** 144501 (2006).

[34] A. R. Thiam, N. Bremond, and J. Bibette, Breaking of an Emulsion under an ac Electric Field, Phys. Rev. Lett. **102,** 188304 (2009).

[35] W. D. Ristenpart, J. C. Bird, A. Belmonte, F. Dollar, and H. A. Stone, Non-coalescence of oppositely charged drops, Nature **461,** 377 (2009).

[36] J. Wang, B. Wang, and H. Qiu, Coalescence and breakup of oppositely charged droplets, Sci. Rep. **4,** 7123 (2014).

[37] D. R. Link, E. Grasland-Mongrain, A. Duri, F. Sarrazin, Z. Cheng, G. Cristobal, M. Marquez, and D. A. Weitz, Electric control of droplets in microfluidic devices, Angew. Chem. Int. Ed. **45,** 2556 (2006).

[38] S. Dash, and S. Mohanty, Dielectrophoretic separation of micron and submicron particles: A review, Electrophoresis **35,** 2656 (2014).

[39] B. Ray, P. D. S. Reddy, D. Bandyopadhyay, S. W. Joo, A. Sharma, S. Qian, and G. Biswas, Surface instability of a thin electrolyte film undergoing coupled electroosmotic and electrophoretic flows in a microfluidic channel, Electrophoresis **32,** 3257 (2011).

[40] D. Bandyopadhyay, P. D. S. Reddy, A. Sharma, S. W. Joo, and S. Qian, Electro-magnetic-field-induced flow and interfacial instabilities in confined stratified liquid layers, Theor. Comput. Fluid Dyn. **26,** 23 (2012).

[41] S. H. Tan, B. Semin, and J.-C. Baret, Microfluidic flow-focusing in ac electric fields, Lab Chip **14,** 1099 (2014).

[42] A. Sharma, J. Chaudhuri, V. Kumar, S. Timung, T. K. Mandal, and D. Bandyopadhyay, Digitization of two-phase flow patterns in a microchannel induced by an external AC field, RSC Adv. **5,** 29545 (2015).

[43] A. Sharma, V. Tiwari, V. Kumar, T. K. Mandal, and D. Bandyopadhyay, Localized electric field induced transition and miniaturization of two-phase flow patterns inside microchannels, Electrophoresis **35,** 2930 (2014).

[44] J. Chaudhuri, S. Timung, C. B. Dandamudi, T. K. Mandal, and D. Bandyopadhyay, Discrete electric field mediated droplet splitting in microchannels: Fission, Cascade, and Rayleigh modes, Electrophoresis **38,** 278 (2017).

[45] S. Timung, J. Chaudhuri, M. P. Borthakur, T. K. Mandal, G. Biswas, and D. Bandyopadhyay, Electric field mediated spraying of miniaturized droplets inside microchannel, Electrophoresis **38,** 1450 (2017).

[46] J. Jang, and S. S. Lee, Theoretical and experimental study of MHD (magnetohydrodynamic) micropump, Sens. Actuators A **80,** 84 (2000).

[47] A. V. Lemoff, and A. P. Lee, An AC magnetohydrodynamic micropump, Sens. Actuators B **63,** 178 (2000).

[48] H. H. Bau, J. Zhong, and M. Yi, A minute magneto hydro dynamic (MHD) mixer, Sens. Actuators B **79,** 207 (2001).

[49] H. H. Bau, J. Z. Zhu, S. Qian, and Y. Xiang, A magnetohydrodynamically controlled fluidic network, Sens. Actuators B **88,** 205 (2003).

[50] P. D. S. Reddy, D. Bandyopadhyay, S. W. Joo, A. Sharma, and S. Qian, Parametric Study on Instabilities in a Two-Layer Electromagnetohydrodynamic Channel Flow Confined Between Two Parallel Electrodes, Phys. Rev. E **83,** 036313 (2011).

[51] J. Zhong, M. Yi, and H. H. Bau, Magneto hydrodynamic (MHD) pump fabricated with ceramic tapes, Sens. Actuators A **96,** 59 (2002).

[52] M. Yi, S. Qian, and H. H. Bau, A magnetohydrodynamic chaotic stirrer, J. Fluid Mech. **468,** 153 (2002).

[53] S. Qian, J. Z. Zhu, and H. H. Bau, A stirrer for magnetohydrodynamically controlled minute fluidic networks, Phys. Fluids **14,** 3584 (2002).

[54] S. Qian, and H. H. Bau, Magneto-hydrodynamics based microfluidics, Mech. Res. Commun. **36,** 10 (2009).

[55] M. C. Weston, M. D. Gerner, and I. Fritsch, Magnetic fields for fluid motion, Anal. Chem. **82,** 3411 (2010).

[56] G. Tomar, D. Gerlach, G. Biswas, N. Alleborn, A. Sharma, F. Durst, S. W. J. Welch, and A. Delgado, Two-phase electrohydrodynamic simulations using a volume-of-fluid approach, J. Comput. Phys. **227,** 1267 (2007).

[57] G. Tomar, G. Biswas, A. Sharma, and A. Agrawal, Numerical simulation of bubble growth in film boiling using a coupled level-set and volume-of-fluid method, Phys. Fluids **17,** 112103 (2005).

[58] D. Jacqmin, Calculation of two-phase navier–stokes flows using phase-field modeling, J. Comput. Phys. **155**, 96 (1999).

[59] Y. Lin, P. Skjetne, and A. Carlson, A phase-field model for multiphase electro-hydrodynamic flows, Int. J. Multiphase Flow **45**, 1 (2012).

[60] J. A. Sethian, and P. Smereka, Level set methods for fluid interfaces, Annu. Rev. Fluid Mech. **35**, 341 (2003).

[61] Y. Lin, Two-phase electro-hydrodynamic flow modeling by a conservative level set model, Electrophoresis **34**, 736 (2013).

[62] J. Zhang, and D. Y. Kwok, A 2D lattice Boltzmann study on electrohydrodynamic drop deformation with the leaky dielectric theory, J. Comput. Phys. **206**, 150 (2005).

[63] See Supplemental Material at http://link.aps.org/supplemental/10.1103/PhysRevApplied.10.034057 for the details of scaling and dimensionless analysis of the governing equations and typical oscillatory motions of different flow features (droplets/plugs and/or slugs) under the influence of time-periodic and oscillating Lorentz force.